



# Structure of the ATP synthase from *Mycobacterium smegmatis* provides targets for treating tuberculosis

Martin G. Montgomery<sup>a,1</sup> , Jessica Petri<sup>a,1</sup>, Tobias E. Spikes<sup>a,1</sup> , and John E. Walker<sup>a,2</sup>

<sup>a</sup>The Medical Research Council Mitochondrial Biology Unit, University of Cambridge, Cambridge CB2 0XY, United Kingdom

Contributed by John E. Walker, October 13, 2021 (sent for review June 28, 2021; reviewed by Thomas M. Duncan and David M. Mueller)

The structure has been determined by electron cryomicroscopy of the adenosine triphosphate (ATP) synthase from *Mycobacterium smegmatis*. This analysis confirms features in a prior description of the structure of the enzyme, but it also describes other highly significant attributes not recognized before that are crucial for understanding the mechanism and regulation of the mycobacterial enzyme. First, we resolved not only the three main states in the catalytic cycle described before but also eight substates that portray structural and mechanistic changes occurring during a 360° catalytic cycle. Second, a mechanism of auto-inhibition of ATP hydrolysis involves not only the engagement of the C-terminal region of an  $\alpha$ -subunit in a loop in the  $\gamma$ -subunit, as proposed before, but also a “fail-safe” mechanism involving the b'-subunit in the peripheral stalk that enhances engagement. A third unreported characteristic is that the fused b $\delta$ -subunit contains a duplicated domain in its N-terminal region where the two copies of the domain participate in similar modes of attachment of the two of three N-terminal regions of the  $\alpha$ -subunits. The auto-inhibitory plus the associated “fail-safe” mechanisms and the modes of attachment of the  $\alpha$ -subunits provide targets for development of innovative antitubercular drugs. The structure also provides support for an observation made in the bovine ATP synthase that the transmembrane proton-motive force that provides the energy to drive the rotary mechanism is delivered directly and tangentially to the rotor via a Grothuss water chain in a polar L-shaped tunnel.

mycobacteria | ATP synthase | structure | regulation | rotary mechanism

The adenosine triphosphate (ATP) synthase in *Mycobacterium tuberculosis* is the antimicrobial target for the treatment of tuberculosis (TB) with the drug bedaquiline (BD), but despite the effectiveness of this drug for treatment of multiple extremely and totally drug-resistant strains of the pathogen, BD resistance has been observed already in clinical isolates (1). Moreover, patients treated with BD have a fivefold higher risk of death than a placebo control group, possibly because of its effects on the human ATP synthase (2). Thus, one possible strategy to combat the growing threat of TB is to identify other inhibitors acting at novel sites of the mycobacterial ATP synthase that could be developed into antibiotics without these side effects. Detailed knowledge of the structure and properties of the enzyme would be helpful in this quest, and the closely related ATP synthase in the nonpathogenic species *Mycobacterium smegmatis* provides an excellent model for the enzyme from the pathogen. Like other mycobacteria, *M. smegmatis* is covered by a complex cell envelope of three distinct layers, consisting of the inner plasma membrane (IPM), the peptidoglycan–arabinogalactan complex, and the outer membrane, which is linked covalently to the arabinogalactan (3). The membrane domain of the mycobacterial ATP synthase is embedded in the IPM, with the catalytic F<sub>1</sub>-domain of the enzyme extending into the bacterial cytoplasm and attached to the membrane domain by a central stalk and a peripheral stalk (PS). As do other ATP synthases in eubacteria, chloroplasts, and mitochondria, the enzyme couples a proton-motive force (pmf) across the IPM generated by respiration to the synthesis in the F<sub>1</sub>-domain of the enzyme of ATP from adenosine

diphosphate (ADP) and phosphate by a mechanical rotary mechanism (4). The mycobacterial rotor consists of a membrane-bound ring of nine c-subunits (5), attached to an elongated central stalk, made of single copies of the  $\gamma$ - and  $\epsilon$ -subunits. This central stalk is common to all F-type ATP synthases and penetrates into the spherical part of the F<sub>1</sub>-domain, an assembly of three  $\alpha$ -subunits and three  $\beta$ -subunits arranged in alternation around the central axis (6). The turning of the asymmetrical rotor brings about a series of conformational changes in the three catalytic sites, which lie at three of the six interfaces between  $\alpha$ - and  $\beta$ -subunits, leading sequentially to the binding of the substrates ADP and phosphate, the formation of ATP, and finally the release of ATP. Three ATP molecules are produced by each 360° rotary cycle (4). The  $\alpha_3\beta_3$ -domain is attached to the a-subunit in the membrane domain by the PS (7). The mycobacterial PS is made of two proteins, b $\delta$  and b'. The b $\delta$ -subunit has been described as a covalent fusion of the separate b- and  $\delta$ -subunits found in many other eubacteria (8). The b'-subunit is orthologous (but not identical) to the b-component of the b $\delta$ -subunit, and both the b-component and the b'-subunit have N-terminal hydrophobic regions, each capable of forming single transmembrane  $\alpha$ -helices. In other bacterial ATP synthases of known structure (9–11), the corresponding  $\alpha$ -helices interact with the final component of the stator, the single a-subunit, and hold it in contact with the rotating c-ring in order to maintain the integrity of the two proton half-channels, thereby maintaining the coupling of

BIOCHEMISTRY

## Significance

As the world tackles the COVID-19 pandemic, other widespread infectious diseases, including tuberculosis (TB), take their toll on humans, and those with TB are more likely to die from COVID-19 infection. Bedaquiline (BD), an anti-TB drug, combats multidrug-resistant *Mycobacterium tuberculosis* by preventing a molecular machine known as the adenosine triphosphate (ATP) synthase from generating ATP, the fuel needed to keep it alive. However, BD-resistant strains of *M. tuberculosis* have arisen. Here, we describe features of the mycobacterial ATP synthase that are not present in the human enzyme. Potentially these features can be exploited for the development of new anti-TB drugs unrelated to BD to prevent and cure TB by inhibiting the formation of ATP by the pathogen.

Author contributions: J.E.W. designed research; M.G.M., J.P., and T.E.S. performed research; M.G.M., J.P., T.E.S., and J.E.W. analyzed data; M.G.M. and J.E.W. wrote the paper; and J.E.W. supervised the project.

Reviewers: T.M.D., State University of New York Upstate Medical University; and D.M.M., Rosalind Franklin University of Medicine and Science.

The authors declare no competing interest.

This open access article is distributed under [Creative Commons Attribution License 4.0 \(CC BY\)](https://creativecommons.org/licenses/by/4.0/).

<sup>1</sup>M.G.M., J.P., and T.E.S. contributed equally to this work.

<sup>2</sup>To whom correspondence may be addressed. Email: walker@mrc-mbu.cam.ac.uk.

This article contains supporting information online at <http://www.pnas.org/lookup/suppl/doi:10.1073/pnas.2111899118/-DCSupplemental>.

Published November 15, 2021.

ATP synthases to the transmembrane pmf. Protons cross the membrane via two half-channels at the interface between the rotating ring and the relatively static stator component of the ATP synthase (4, 12, 13), and they provide the energy from the pmf required to generate the turning of the rotor. Previously, we have described the atomic structure of the F<sub>1</sub>-catalytic domain of the ATP synthase from *M. smegmatis* determined by X-ray crystallography (6), and recently an independent structure has been described of the entire mycobacterial complex determined by electron cryomicroscopy (cryo-EM) of purified single particles of the enzyme inhibited by BD (14). In this analysis, three catalytic states of the enzyme were resolved corresponding to the same inhibited catalytic state in the three different positions relative to the single PS. In addition, a novel method of auto-inhibition was suggested by the association of one of the extended structures in the C-terminal region of the  $\alpha$ -subunits with a loop region in the  $\gamma$ -subunit. Both the C-terminal extension in the  $\alpha$ -subunits and the additional loop in the  $\gamma$ -subunit are conserved in mycobacterial ATP synthases but are not found elsewhere among eubacterial, chloroplast, or mitochondrial ATP synthases.

Here, we describe an independent structural analysis of the mycobacterial enzyme inhibited by BD. This structure not only confirms many of the features in the earlier structures of the enzyme (6, 14) but also it provides evidence of other highly significant features that have not been described before that are crucial for understanding the mechanism and regulation of the mycobacterial enzyme. Most notably, we have resolved not only the three main states in the catalytic cycle but also eight additional substates, thereby elaborating structural and mechanistic changes that occur during a 360° catalytic cycle. Second, the auto-inhibitory mechanism has been extended to involve not only the C-terminal region of an  $\alpha$ -subunit and a loop in the  $\gamma$ -subunit, as proposed before (14), but also the b'-subunit in the PS. Third, we have demonstrated that the fused b $\delta$ -subunit contains a duplicated domain in its N-terminal region where the two copies of the domain participate in similar modes of attachment of the two of three N-terminal regions of the  $\alpha$ -subunits. Another significant feature of the structure is that it provides further support for an observation made in the bovine ATP synthase that the transmembrane pmf that provides the energy to turn the enzyme's rotor is delivered directly and tangentially to the rotor via a Grothuss water chain in a polar L-shaped tunnel formed at the inlet half-channel (15). Subsequently, a similar mechanism has been proposed to operate in the yeast V-type ATPase, based on a structure determined at ca. 2.7 Å, where ordered chains of water molecules were observed in both the inlet and outlet half-channels (16)

## Results and Discussion

**The Structure of Mycobacterial ATP Synthase.** Single particles of the ATP synthase from *M. smegmatis* purified in the presence of detergent (SI Appendix, Fig. S1 and Table S1) and inhibited with BD were subject to cryo-EM analysis. A total of 63 maps and 27 models of the enzyme were resolved and refined with resolutions ranging from 2.11 to 4.15 Å (SI Appendix, Figs. S2 and S3 and Tables S2 and S3). The best-resolved model, that of substate S1a (see below; Protein Data Bank [PDB] ID code 7NJK) is at a resolution of 2.5 to 3.4 Å. For the quality of the electron density of each subunit, see SI Appendix, Fig. S4. The model of substate S1a (Fig. 1 and Movie S1) contains the following residues:  $\alpha_E$  5 to 21, 29 to 406, 411 to 521;  $\alpha_{TP}$  5 to 21, 29 to 406, 411 to 521;  $\alpha_{DP}$  6 to 406, 413 to 521, 527 to 545;  $\beta_E$  8 to 471;  $\beta_{TP}$  7 to 475;  $\beta_{DP}$  8 to 475;  $\gamma$  3 to 213, 220 to 304;  $\epsilon$  3 to 120; a 10 to 247; b $\delta$  1 to 162, 169 to 444; b' 22 to 166; c 3 to 86 (in all nine copies). Each nucleotide binding site in the three  $\alpha$ -subunits and in subunit  $\beta_{TP}$  is occupied by an ATP molecule

with an accompanying Mg<sup>2+</sup> ion, while the site in subunit  $\beta_{DP}$  has ADP and an accompanying Mg<sup>2+</sup> ion. The sixth nucleotide binding site in subunit  $\beta_E$  contains an ADP molecule with neither accompanying Mg<sup>2+</sup> nor phosphate (see SI Appendix, Fig. S5). For comparison, in a similar cryo-EM analysis of single particles of the same mycobacterial ATP synthase, 12 maps and models were resolved with resolutions ranging from 3.2 to 3.7 Å (14). In that study, the best-resolved model (PDB ID code 7JGA, 3.2 Å) has the following residues:  $\alpha_E$  7 to 520;  $\alpha_{TP}$  9 to 22, 29 to 515, 533 to 546;  $\alpha_{DP}$  8 to 22, 28 to 545;  $\beta_E$  8 to 471;  $\beta_{TP}$  8 to 471;  $\beta_{DP}$  8 to 471;  $\gamma$  4 to 164, 178 to 213, 220 to 303;  $\epsilon$  3 to 119; a 31 to 113, 123 to 246; b $\delta$  1 to 157, 169 to 331, 337 to 444; b' 24 to 164; c 5 to 85 (in all nine copies). The occupancy of nucleotides is as follows (PDB ID code 7JGA): ATP is present in all three  $\alpha$ -subunits, and ADP is present in  $\beta_{TP}$  with a Mg<sup>2+</sup> ion coordinated by the nucleotide and a threonine residue ( $\alpha$ Thr179 or  $\beta$ Thr167) and water molecules in each case. Neither  $\beta_{DP}$  nor  $\beta_E$  has a bound nucleotide, probably as there were no exogenous nucleotides present throughout the purification process. A phosphate has been modeled in  $\beta_E$  at the top of the binding site near to Glu196, Asp254, and Arg376. One major difference is that in the prior study (14) BD was well-resolved bound to the c<sub>9</sub>-ring at the interface with the a-subunit. In the current study, the concentration of BD employed was almost an order of magnitude lower (25  $\mu$ M instead of 200  $\mu$ M), and this lower concentration proved to be suboptimal for the detection of the BD itself, as the drug was present in only a minority of particles. Therefore, in the various states and substates (see below) the density for BD is highly variable. Also, in the earlier study, a different detergent was used in the isolation of the intact particles of the enzyme, and that also may have influenced the binding of BD to the enzyme. While it is possible that differing detergent, BD, or nucleotide concentrations in the enzyme preparations may be responsible for the wider range of substates observed, each of the substates in the current work have exactly the same nucleotide occupancies and this is mirrored in recently reported substates in the *Escherichia coli* enzyme (17), suggesting that the resolved substates are nucleotide-independent. It is also possible that further refinement of the particle classes in the previous data (14) could reveal some or all of the substates presented here. However, in the current work, by combining the membrane domains of all of the particles, bound BD could be modeled in the same position as previously reported in close proximity to the N-terminal region of aH5 of the c-subunit in a position that would inhibit ATP synthesis (see SI Appendix, Fig. S6). This position is the “lagging” site (14). In some reconstructions, partial nonprotein densities were observed at the opposite side of the a-c interface in close proximity to the C-terminal region of aH5 as in the prior publication. However, the densities were poorly defined and it would be tenuous, in the absence of previously published results (14), to assign them definitively as BD molecules. Similar to the prior study (14), the electron density maps for each of states S1 to S3 has density for both tethered and untethered forms, and hence those particle classes contain enzymes that are auto-inhibited and others that are not inhibited by this mechanism. In the tethered forms the mycobacterial-specific extensions of the  $\alpha$ -subunit make contact with the  $\gamma$ -subunit. In the untethered forms, these regions are disordered in the reconstructions and are presumably freely moving in the adjacent aqueous environment.

**Catalytic States and Substates.** The three catalytic sites in the F<sub>1</sub> domain of ATP synthases are arranged at 120° intervals around the rotor, and active ATP synthases have been defined in three main states distinguished from each other by the position of the rotor relative to the stator. Extensive classification of the data for the mycobacterial ATP synthase revealed the presence of

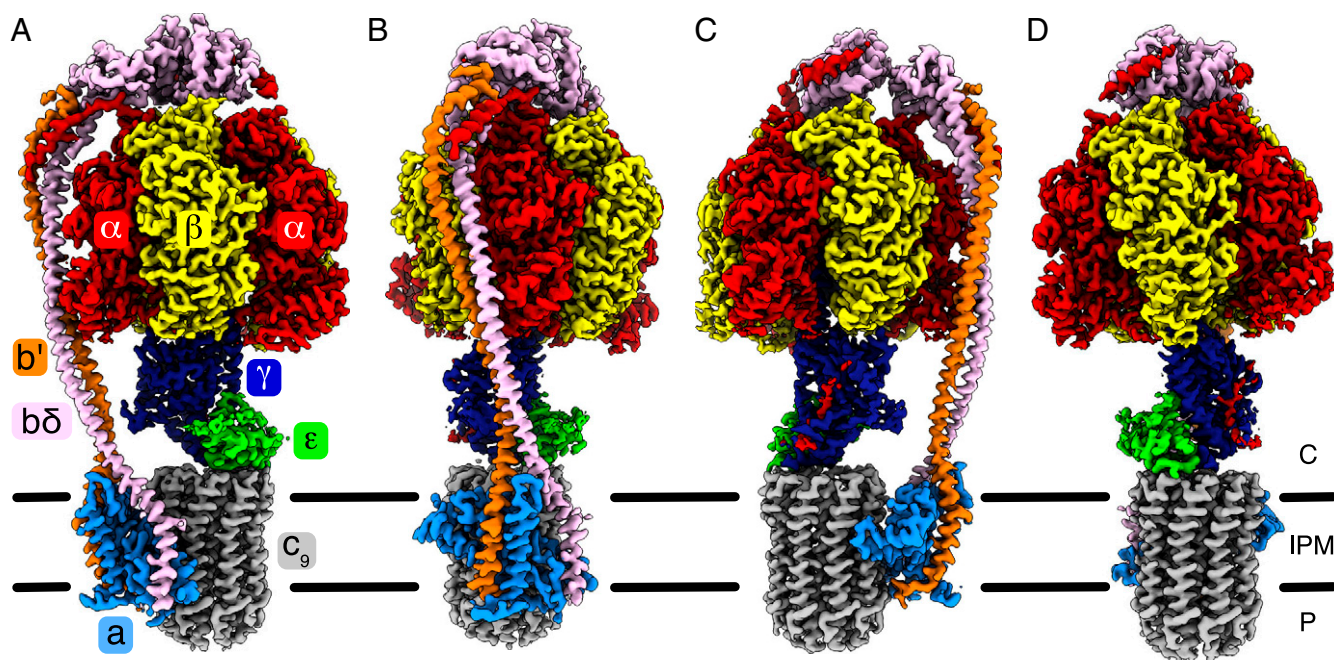


**Fig. 1.** The structure and subunit composition of ATP synthase from *M. smegmatis*. (A–D) Four views of the electron density of the intact enzyme in state S1a (EMD-12377). The colors corresponding to each subunit are indicated in A. In B–D, the views are rotated by 90° from left to right about the vertical axis running through the central stalk and the center of the  $c_9$ -ring. The mycobacterial ATP synthase consists of three copies of the  $\alpha$ -subunit, with an extended C terminus unique to *Mycobacteria*; three copies of the  $\beta$ -subunit; nine copies of the  $c$ -subunit; and one copy each of the  $\gamma$ -,  $\epsilon$ -,  $a$ -,  $b'$ -, and  $b\delta$ -subunits. The latter is also unique to *Mycobacteria* and comprises a canonical  $b$ -subunit fused to a canonical  $\delta$ -subunit via an additional bundle of seven  $\alpha$ -helices. The black bars represent the IPM. Protons are translocated from the periplasm (P) to the cytoplasm via the interface between  $a$ - and  $c$ -subunits.

not only the three main states referred to as S1, S2, and S3 but also of substates within them (Fig. 2). Substates S1a to S1e are in S1, and S3a to S3c are in S3. Two further substates were detected in state S1, and one in state S2, but the number of particles collected in each instance was insufficient to allow accurate models to be built (SI Appendix, Fig. S3). Alignment of the substates in S1 and S3 with the three states observed previously via their  $a$ -subunits showed that substate S1a (PDB ID code 7NJK) closely matches the earlier state 1 (PDB ID code 7JG5) and S2 (PDB ID code 7NJP) is closely similar to the previous state 2 (PDB ID code 7JG6). In their membrane domains, substates S3a (PDB ID code 7NJQ), S3b (PDB ID code 7NJR), and S3c (PDB ID code 7NJS) are similar to the earlier state 3 (PDB ID code 7JG7), but there are significant deviations in the  $F_1$  and PS domains (SI Appendix, Fig. S7).

The main differences between the substates within each state are that the positions of the PS and  $F_1$  domains vary such that the  $F_1$ -domain (including the  $\alpha$ -helical coiled-coil of the  $\gamma$ -subunit) appears to pivot around the PS during the catalytic cycle (Movies S2 and S3). Pivot points are located around residues 59 to 66 in the  $b$ -subunit, residues 34 to 41 in the  $b\delta$ -subunit, and residues 43 and 233 in the  $\gamma$ -subunit (SI Appendix, Figs. S8 and S9). However, alignment of the substates via the “crown” in the  $F_1$ -domain shows that they have identical nucleotide occupancies and that the position of the  $\gamma$ -subunit is also maintained. Alignment of the substates via the  $a$ -subunit demonstrates that the  $c_9$ -rings and the membrane  $\alpha$ -helices of the  $a$ -,  $b$ -, and  $b\delta$ -subunits of the substates are in identical positions, as are the  $\epsilon$ -subunits, and in some instances the lower part of the  $\gamma$ -subunit.

As in all other F-ATPases, the  $F_1$  catalytic domain has threefold pseudosymmetry with each catalytic interface of the  $\alpha$ - and  $\beta$ -subunits separated by 120°. However, similar to the F-ATPases from *Paracoccus denitrificans* and *Spirulina platensis* which, respectively, have  $c_{12}$  and  $c_{15}$  rotor rings (9, 18), the

mycobacterial  $c_9$ -ring has a symmetry related to that of the  $F_1$ -domain, whereas in other species where the number of  $c$ -subunits is not divisible by 3 there is a “symmetry mismatch” between the catalytic and  $c$ -ring rotor domains. This symmetry mismatch has been invoked as being part of a mechanism for storing energy transiently in the  $\gamma$ -subunit as the ring rotates (4). This energy is released subsequently in quanta to generate the observed stepping of the rotor (the  $\gamma$ -subunit) in the  $F_1$ -region. Despite the symmetry correspondence between its  $F_1$  and  $c$ -ring domains in the structure of the enzyme from *M. smegmatis*, a symmetry mismatch between the two domains persists here also. The presence of this mismatch is demonstrated by catalytic states S1 to S3, which do not display threefold symmetry and are not separated from each other by 120° (Fig. 3). Thus, as the structures of  $\gamma$ -subunits are highly conserved, it appears that there is a conservation of an energetic mismatch between the two domains that is independent of symmetry. Thus, as illustrated in Fig. 3 and Movie S4, by using the  $c$ -subunit directly under the  $\epsilon$ -subunit as a marker, the rotation of the ring can be tracked through the substates (Fig. 3A). In S1, the rotor turns almost one  $c$ -subunit onward (ca. 40°) from S1a (Fig. 3B), in the direction of synthesis (anticlockwise from above) to substate S1b, which also moves the  $\gamma$ - and  $\epsilon$ -subunits relative to the other states. Further round from S1b by ca. 2° lie S1c to S1e, which have similar  $c$ -ring positions to each other (Fig. 3C), but there are large differences in the  $F_1$  domain and in the PS. The positions of the top of the PS suggest that the order of procession is S1a > S1b > S1e > S1d > S1c. As the inhibitory tether is attached in some of the particles, this movement of the rotor in S1a and S1b may also be responsible for additional differences in the  $F_1$ -domain and the PS compared to S1c to S1e. In S2 (where there are no resolved substates) the  $c$ -ring has traveled two  $c$ -monomers further round (ca. 120°), and in state 3 substates S3a to S3c have all traveled on to approximately the same position, four  $c$ -monomers (or ca.

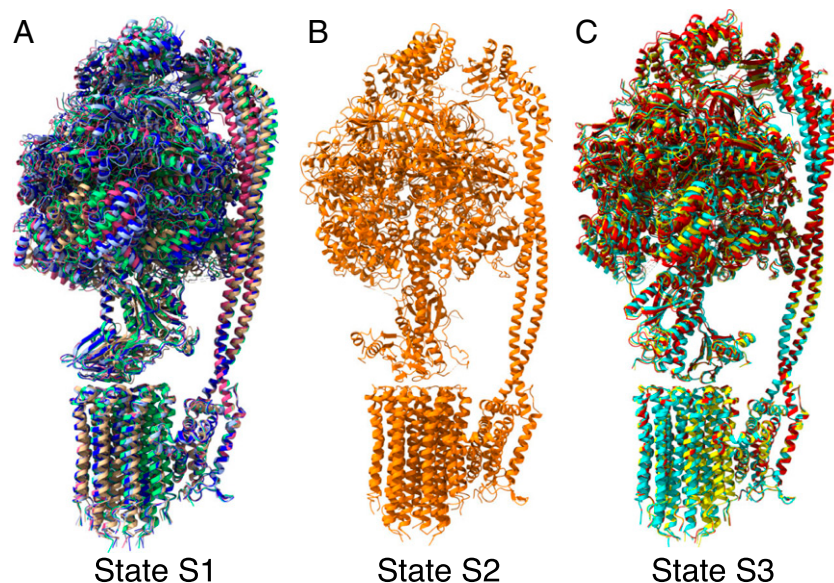


**Fig. 2.** Structures of states and substates in the catalytic cycle of the ATP synthase from *M. smegmatis*. (A–C) The structures of the three main states, S1 to S3, defined by the position of the rotor relative to the stator. Each 360° rotary cycle is composed of the transitions S1 to S2, S2 to S3, and S3 to S1. In state S2, the rotor has turned 120° relative to state S1 and in state S3 by 120° relative to state S2. In states S1 and S3, substates S1a to S1e and S3a to S3c, respectively, were resolved. (A) Superimposition of substates S1a to S1e, colored tan, green, magenta, pale blue, and dark blue, respectively. (B) State S2. (C) Superimposition of substates S3a to S3c, colored yellow, cyan, and red, respectively. The substates are aligned via their  $\alpha$ -subunits. In states S1 and S3, the F<sub>1</sub> and PS domains occupy a variety of positions (although in an alignment of the substates via the crown of the F<sub>1</sub>-domain, the nucleotide occupancies of the F<sub>1</sub> domains are identical and the position of the  $\gamma$ -subunit is approximately constant). In substate S1a, the rotor has turned one c-subunit onward in a hydrolytic direction compared to S1b to S1e (see Fig. 3).

280°) further on (Fig. 3 D and E). Again, the position of the PS suggests that the order of substates is either S3c > S3a > S3b or S3b > S3a > S3c. Thus, the order of all the resolved substates in the synthesis direction is either S1a > S1b > S1e > S1d > S1c > S2 > S3c > S3a > S3b (Movie S2) or S1a > S1b > S1e > S1d > S1c > S2 > S3b > S3a > S3c (Movies S3). Among the substates reported in the ATP synthase from *E. coli* (17), one substate, S1a, also corresponds to a rotor turn of one c-subunit. However, relative to the mycobacterial enzyme, the accompanying movement in the  $\gamma$ - and  $\epsilon$ -subunits is much less, probably because the *E. coli*  $\epsilon$ -subunit is in the inhibitory “up” position (19) where its C-terminal domain occupies the cavity next to the  $\alpha$ -helical coiled-coil of the  $\gamma$ -subunit in F<sub>1</sub>-domain of the enzyme, and similarly for the ATP synthase from *Geobacillus stearothermophilus* (11). In the mycobacterial ATP synthase it is not known whether the  $\epsilon$ -subunit, which is observed in the “down” position in the structure, can also assume the “up” position, but there is no evidence that it does so (20, 21). Thus, it appears that the mycobacterial PS, as proposed in other ATP synthases where there is a mismatch of symmetries between F<sub>1</sub> and c-ring domains (4, 22), also acts as a spring that stores and then releases energy to generate the steps in the F<sub>1</sub>-domain during rotation (17, 23) (see SI Appendix, Figs. S10 and S11 and Movies S2, S3, and S5, illustrating the transitions during synthesis, in Movies S2 and S3, and in hydrolysis, in Movie S5, by the ATP synthases from *M. smegmatis*).

**Auto-Inhibition of ATP Hydrolysis.** The structure of the ATP synthase from *M. smegmatis* suggests a tether mechanism for the inhibition of ATP hydrolysis, and of the accompanying reversal of the direction of turning of the rotor and expulsion of protons from the bacterial cytoplasm that would happen when the pmf is disrupted, for example under anaerobic conditions (14). This mechanism has two elements based upon structural features that are unique to the mycobacterial ATP synthases. In the first element (Fig. 4 A–F and SI Appendix, Fig. S12) described before (14), residues 520 to 548 extend from the C-terminal

region of  $\alpha$ -subunits and provide a “hook” which catches into a “loop” provided by residues 212 to 220 in the lower globular domain of the  $\gamma$ -subunit, thereby tethering the stator and rotor together and inhibiting rotation (see also Movie S6). An important feature of this tether mechanism is that it is unidirectional, operating only in the hydrolytic direction of rotation when their interacting surfaces have complementary charges (Fig. 4 C–E). In contrast, in the synthetic direction, as the interacting surfaces are both negatively charged they will repel each other, thereby preventing an inhibited complex from forming. This part of the tether mechanism is consistent with the observation that the treatment of the F<sub>1</sub>-ATPase from *M. smegmatis* with trypsin activates its ATP hydrolytic activity as trypsinolysis removes residues 543 to 548 of the  $\alpha$ -subunits and disrupts the loop region by cleaving the  $\gamma$ -subunit after residue 219 (6) (see SI Appendix, Fig. S13). The second element of this inhibitory mechanism depicted in Fig. 4 G–I and SI Appendix, Figs. S14 and S15 has not been described previously, and it provides a “fail-safe” device. During rotation through S1 in either direction, the  $\gamma$ -subunit approaches very close to the PS at b'Arg72, and potentially a salt bridge could form between this residue and either  $\gamma$ Asp170 or  $\gamma$ Asp171. Unlike the tether, which can be formed in any of S1 to S3, this feature can form only in S1, when, during rotation, the  $\gamma$ -subunit comes sufficiently close to the PS for a salt bridge to form. Hence, if the hook fails to engage in the loop and form the tether in S2 and S3, in S1 the proximity of b'Arg72 and  $\gamma$ Asp170 plus  $\gamma$ Asp171, and the formation of the salt bridge, will increase the likelihood of the hook's engaging in the loop in this state as the hook would be prevented from slipping around the  $\gamma$ -subunit because of the proximity of residues  $\gamma$ 168 to 175 to the PS. In *M. tuberculosis*, residues 168 to 175 EGDDAGAD in *M. smegmatis* are replaced by residues 168 to 174 GEDQRS, and b'Arg72 in *M. smegmatis* is substituted by b'Lys72 in *M. tuberculosis*. Although the changed sequences in *M. tuberculosis* could conceivably affect the fold of the loop and the possibility of forming a salt bridge with b'Lys72, it is highly likely that this region of the  $\gamma$ -subunit

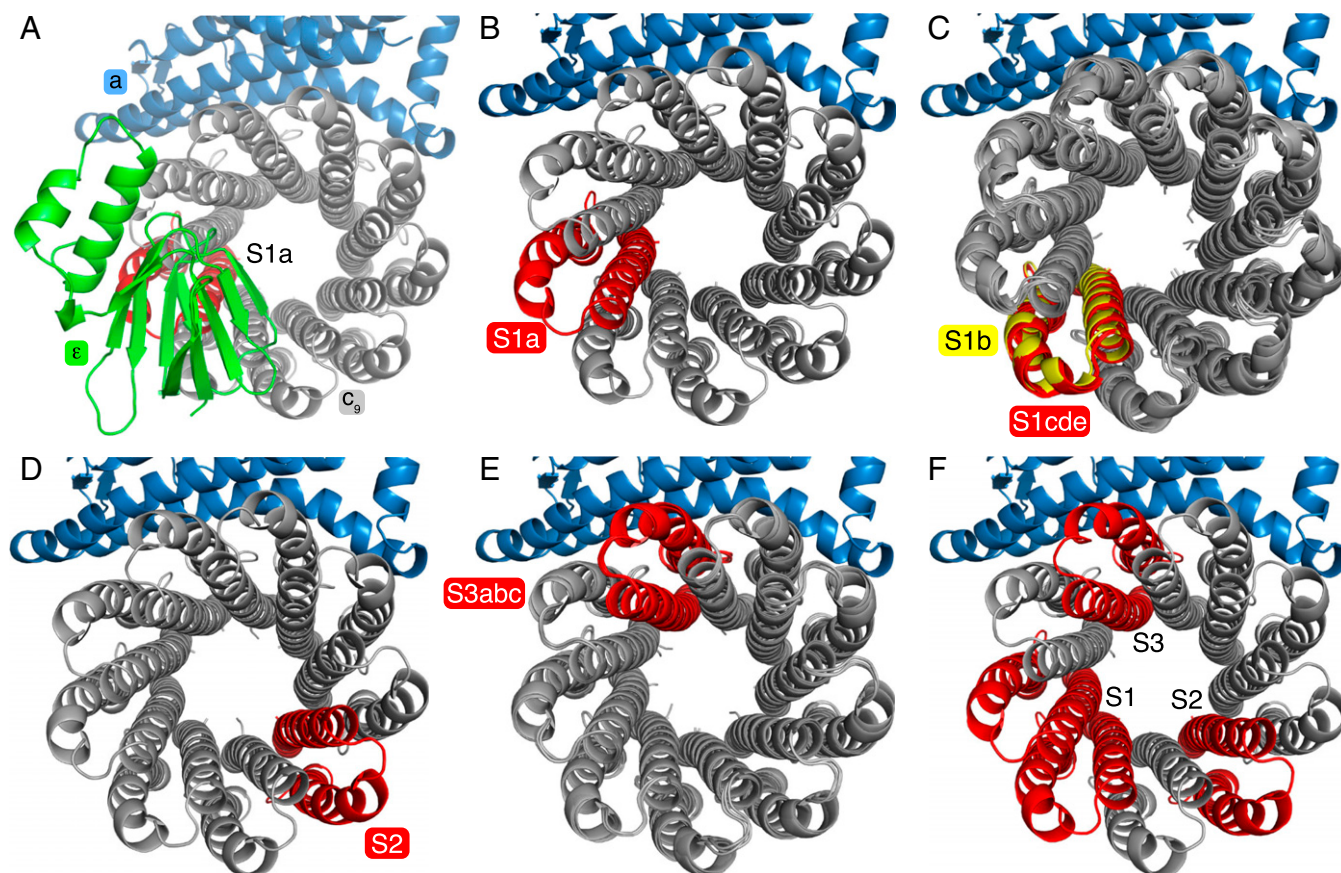


**Fig. 3.** Symmetry mismatch in the substate rotors. By aligning all of the substate models via their a-subunits, the rotation of the  $c_9$ -ring was tracked through the substates via the c-subunit located directly beneath the  $\beta$ -sheet domain of the  $\epsilon$ -subunit. (A) View from above substate S1a with the  $\epsilon$ -, a-, and c-subunits colored green, sky blue, and gray, respectively, with the c-subunit directly beneath the  $\epsilon$ -subunit in red. (B–E) Similar views of substates with the  $\epsilon$ -subunit removed and the equivalent c-subunit in each substate colored. (B) Substate S1a. (C) Overlays of the c-rings from substates S1b to e. In these substates, the equivalent c-subunits have rotated approximately one c-monomer further round in the synthesis direction (anticlockwise). In C, the highlighted c-subunit of S1b (yellow) has rotated by ca.  $40^\circ$ , whereas in substates S1c to S1e it has rotated by ca.  $42^\circ$  to approximately the same position shown in red. In D, state S2 has rotated two c-monomers further round with a corresponding rotation of ca.  $120^\circ$ . In E, substates S3a to c have rotated by a further three c-monomers (ca.  $280^\circ$ ). (F) Summary of the positions of the c-rings in the three main states S1, S2, and S3.

would still come into contact with the PS and that the “fail-safe” mechanism will operate in the pathogen also. These observations expand on preliminary biochemical data that residues  $\gamma$  168 to 175 are involved in regulation of the enzyme (24). These features are not present in the ATP synthases from either *E. coli* (see *SI Appendix*, Fig. S15) or *G. stearothermophilus* where, during a  $360^\circ$  rotary cycle, the  $\gamma$ -subunits do not come close to the PS. In the prior structure of the ATP synthase from *M. smegmatis*, residues 164 to 177 were disordered.

**The PS.** The PS is a key component of the enzyme’s stator joining the external surface of the  $\alpha_3\beta_3$ -spherical component of the catalytic domain to the a-subunit in the membrane domain, thereby helping to ensure the maintenance of the contact between the membrane domains of the rotor and the stator during catalysis (4). The simplest examples are found in some eubacteria and chloroplasts where the N-terminal domain of the  $\delta$ -subunit is attached noncovalently to N-terminal extensions of the three  $\alpha$ -subunits, and its C-terminal domain forms other noncovalent interactions with the C-terminal regions of two identical b-subunits (as in *E. coli*, for example) or two nonidentical but orthologous b- and b'-subunits, as in cyanobacteria (25, 26) and chloroplasts (27), for example. Metazoan and fungal mitochondrial ATP synthases have a related but more complex PS where the OSCP (oligomycin sensitivity conferral protein) subunit,

which is orthologous to the bacterial  $\delta$ -subunits (28), also binds to the N-terminal regions of the three  $\alpha$ -subunits and joins to a long and complex  $\alpha$ -helical structure that extends to and penetrates the inner mitochondrial membrane, where it helps to hold the a-subunit of the stator against the c-ring of the rotor. The composition and structure of the PS in mycobacteria has similarities to the PS regions in other prokaryotic ATP synthases, but there are significant differences. In the structure of the *M. smegmatis* ATP synthase, the PS is a complex of a single b'-subunit (similar to b'-subunits in bacteria [see *SI Appendix*, Fig. S16] and chloroplasts) and the unique b $\delta$ -subunit. This b $\delta$ -subunit has been described previously as a fusion protein with a linking region between the C-terminal region of the b-subunit and the N-terminal region of the  $\delta$ -subunit with the  $\delta$ -subunit component bound noncovalently to the N-terminal regions of the three  $\alpha$ -subunits (14). However, as described below, this description is inaccurate. In the current structure, the b $\delta$ -subunit consists of 16  $\alpha$ -helices with a  $\beta$ -strand separating b $\delta$ H14 and b $\delta$ H15, with three additional  $\beta$ -strands between b $\delta$ H15 and b $\delta$ H16 (Fig. 5 A and B). These structural elements form three separate domains. The N-terminal “b” domain is similar to those of other bacterial b-subunits (see *SI Appendix*, Fig. S17). Its structure consists of b $\delta$ H1 to b $\delta$ H3 and is similar to the equivalent region of a canonical bacterial b-subunit with b $\delta$ H1 spanning the bacterial IPM.  $\alpha$ -Helix b $\delta$ H1 and the equivalent, but nonassociated, b/H1 bind

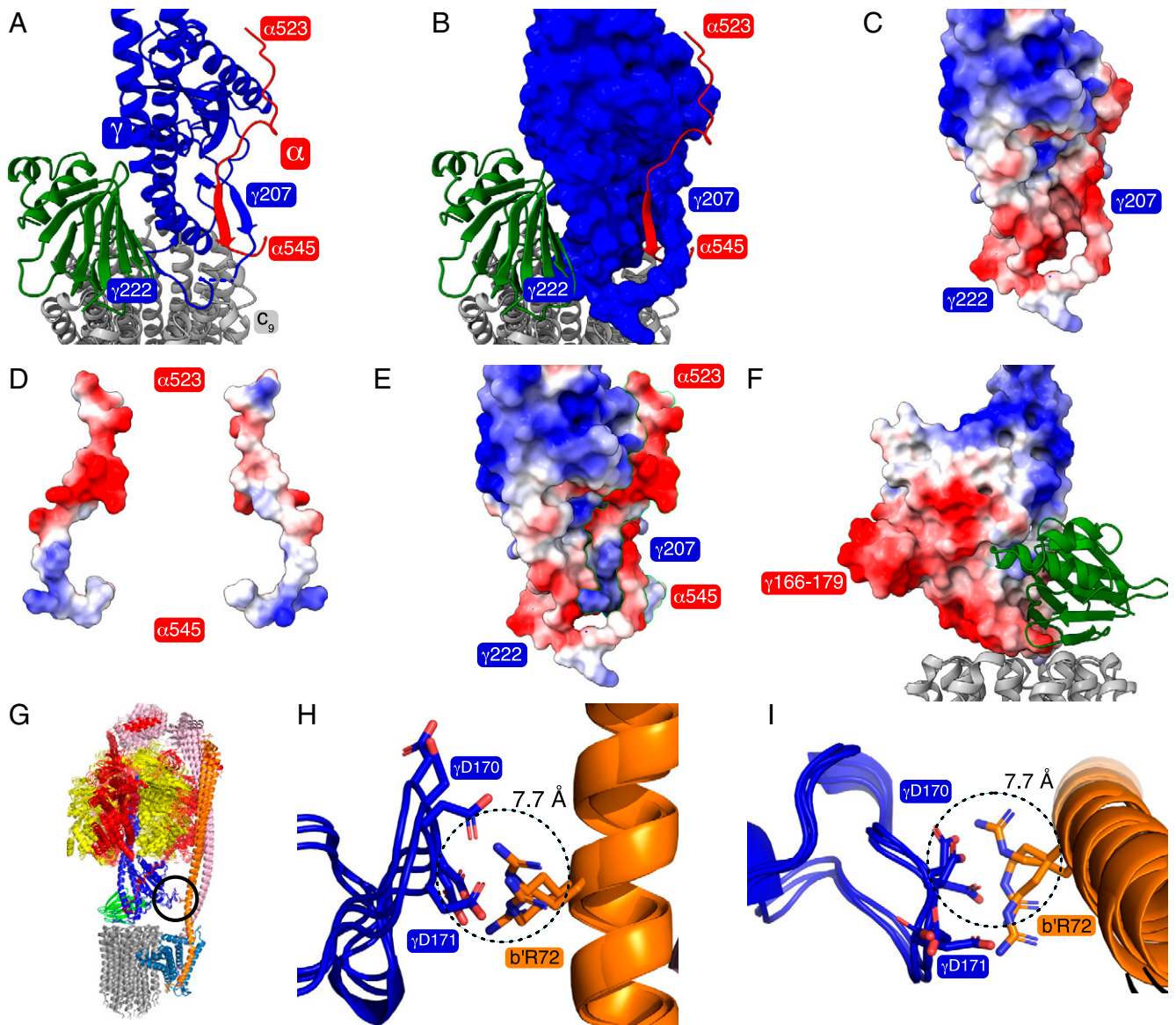


**Fig. 4.** Auto-inhibition of hydrolysis in the ATP synthase from *M. smegmatis*. (A and B) The extended “hook” provided by residues in the C-terminal region of an  $\alpha$ -subunit (red) engaged in a “loop” provided by residues 205 to 227 of a  $\gamma$ -subunit (blue). The  $\epsilon$ -subunit (green) is bound to this region of the  $\gamma$ -subunit and attaches the central stalk (subunits  $\gamma$  and  $\epsilon$ ) to the  $c_9$ -ring (gray). Together, the  $\gamma$ - and  $\epsilon$ -subunits plus the  $c_9$ -ring constitute the enzyme’s rotor. The subunits are depicted in cartoon representation, except for the  $\gamma$ -subunit in B, which is in space-filling format. (C–E) The electrostatic potentials of the surfaces of the elements of the hook and loop mechanism of inhibition of ATP hydrolysis. (C) The loop. (D) The two opposing surfaces of the “hook” with the positively charged surface that engages the negatively charged “loop” during ATP hydrolysis on the left. (E) The hook engaged in the loop. (F) During ATP synthesis, the positively charged face shown on the right is presented to the positively charged external surface of the “loop” and is repelled. Hence, the inhibitory mechanism is unidirectional. In A–F, the model of the rotor in state 3 is depicted (PDB ID code 7NKO). (G–I) The “fail-safe” mechanism augmenting the “hook–loop” catch mechanism involving an interaction between residues  $\gamma$ 166 and 179 and b’Arg72. (G) The encircled region denotes the “fail-safe” device. It occurs between the rotor and the stator in state 1, and especially in substates S1c, S1d, and S1e, which are shown in cartoon format superimposed via their a-subunits. (H and I) Close-up views from the side and from above, respectively, showing in stick representation the interaction between negatively charged residues  $\gamma$ Asp170 and  $\gamma$ Asp171 with positively charged b’Arg72. The diameter of the dotted circle is 7.7 Å corresponding to the distance between the C $\alpha$  atoms of  $\gamma$ Asp171 and bArg72 in substate S1d.

to separate regions of the a-subunit and help to maintain the integrity of the transmembrane proton pathway.  $\alpha$ -Helix b $\delta$ H2 extends vertically from the IPM and then runs along the external surface of the F<sub>1</sub>-domain, and finally links to b $\delta$ H3, which extends the PS to the top of the F<sub>1</sub>-domain. Then, b $\delta$ H4 to b $\delta$ H8 form a separate domain, named the “linking domain,” which is attached to b $\delta$ H9 in the third domain, named “the  $\delta$ -domain,” consisting of b $\delta$ H9 to b $\delta$ H16. The  $\delta$ -domain is similar to the canonical  $\delta$ -subunits in other eubacteria (SI Appendix, Fig. S18). However, a feature not remarked on previously is that the b $\delta$ H4

to b $\delta$ H8 linking domain can be superimposed onto the  $\delta$ -domain by a clockwise rotation of *ca.* 120° (see Fig. 5C and Movie S7). Therefore, the  $\delta$ - and linking domains appear to have arisen by a process that involves a gene duplication event at some point during evolution. The amino acid sequences of the two domains are *ca.* 20% identical, and a further 20% of residues are substituted conservatively (SI Appendix, Fig. S19). In the structure, there was no density for residues 1 to 21 of subunit b’ although they are present in the assembled enzyme (SI Appendix, Table S1). Thus, the b $\delta$ -subunit has two structurally related domains and each

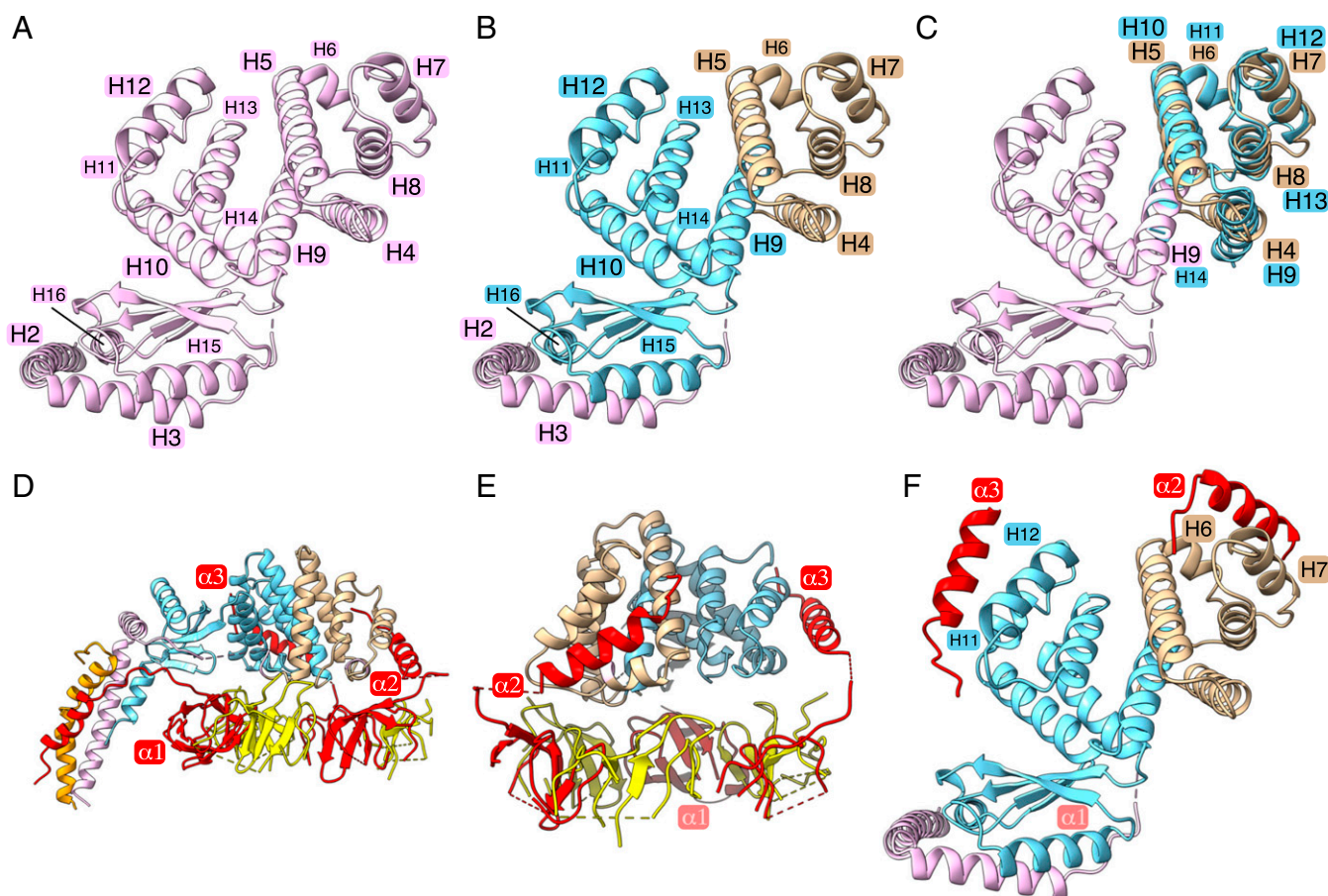


**Fig. 5.** Structure of the  $b\delta$ -subunit and its interactions with  $\alpha$ -subunits in the ATP synthase from *M. smegmatis*. (A) The  $b\delta$ -subunit (pink) viewed from above the crown of the  $F_1$ -domain toward the IPM consists of 16  $\alpha$ -helices,  $b\delta H1$  to  $b\delta H16$ , with a single intervening  $\beta$ -strand between  $b\delta H14$  and  $b\delta H15$  and three additional  $\beta$ -strands between  $b\delta H15$  and  $b\delta H16$ . In this view,  $b\delta H1$ , which traverses the IPM, is not visible. (B) The three domains of the  $b\delta$ -subunit, with the N-terminal “b”-domain (pink) consisting of  $b\delta H1$  to  $b\delta H3$ , followed by the central “linking domain” (tan) consisting of  $b\delta H4$  to  $b\delta H8$ , and the C-terminal “ $\delta$ ”-domain (pale blue), consisting of  $b\delta H9$  to  $b\delta H16$ . (C) Superimposition of the “ $\delta$ -domain” (pale blue) and the “linking domain” (tan) by a clockwise rotation of ca.  $120^\circ$  (see [Movie S7](#)). (D and E) Interactions of the N-terminal  $\alpha$ -helical regions (labeled  $\alpha 1$ ,  $\alpha 2$ , and  $\alpha 3$ ) of the three  $\alpha$ -subunits (red) with the  $b\delta$ -subunit. Elements of the  $\alpha$ - and  $\beta$ -subunits in the “crown” region of the  $F_1$ -domain are colored red and yellow, respectively. In D part of the b-subunit (residues 130 to 166) is orange. In E relative to D, the view has been rotated by  $90^\circ$  toward the viewer. (F) The same view as in A–C illustrating the similarity of the modes of binding of N-terminal regions  $\alpha 2$  and  $\alpha 3$  to the “linking domain” (tan) and the “ $\delta$ -domain” (pale blue), respectively. In D, the N-terminal region  $\alpha 1$  is bound close to the PS and interacting with  $b\delta H2$ ,  $b\delta H16$ , the immediately preceding  $\beta$ -strand, and the

binds to the N-terminal region of an  $\alpha$ -subunit (subunits  $\alpha 2$  and  $\alpha 3$ ) in a similar fashion with the third  $\alpha$ -subunit attached by a different mode (Fig. 5 D–F). In other bacterial species, the mode of binding of the N-terminal region  $\alpha 2$  differs from the mode of binding in the *M. smegmatis* ATP synthase, as illustrated in [SI Appendix, Fig. S20](#). At present, it is not clear what advantage, if any, is associated with the similarity of the modes of binding of N-terminal regions of  $\alpha 2$  and  $\alpha 3$ .

**Proton Translocation.** One of the most important and fundamental mechanistic features resolved in the recent structure of the dimeric bovine ATP synthase is the Grothuss chain of water molecules in the inverted L-shaped proton inlet half-channel that leads from the intermembrane space of the mitochondria to the essential  $\gamma$ -carboxylate found on the c-subunit lying at the end of this half-channel (15). This Grothuss water chain allows the full effect of the transmembrane proton motive force to be applied directly and tangentially to the c-ring to drive its rotation in the direction required for ATP synthesis. In the mycobacterial enzyme, this inverted L-shaped half-channel is clearly present (Fig. 6), but the water molecules that form the

Grothuss chain were not resolved. The mycobacterial inlet channel in the a-subunit contains the polar residues aHis12, aHis15, aHis16, aAsp30, aAsn104, aGln112, aAsp117, aGlu122, aLys125, aGln192, aLys219, aAsp222, and aGln229, which are probably involved in the coordination of the water molecules that form the Grothuss chain ([SI Appendix, Fig. S21](#)). The proton inlet pathway then passes through a small aperture between  $\alpha$ -helices aH5 and aH6 formed by residues aGly196 and aAsp222 into the interface between the a-subunit and the c-ring. A gap leading to this channel is plugged by residue Gln7 of the b-subunit and another, between aLeu111 and aTyr124, leads to the membrane and is presumably blocked by lipids ([SI Appendix, Figs. S22 and S23](#)). As in the bovine and other ATP synthases, the outlet channel is more open and funnel-shaped. Polar residues aHis146, aArg153, aLys161, aHis166, aAsn174, aGlu177, aGlu178, aLys181, aSer184, aTyr240, aGln243, and aGlu246 are found in this region. Although the positions and overall polarities of the inlet and outlet half-channels are conserved in mitochondrial and bacterial ATP synthases, in general specific polar residues are not conserved, with the exception of aArg188, and aGly196 found at the aperture between the two

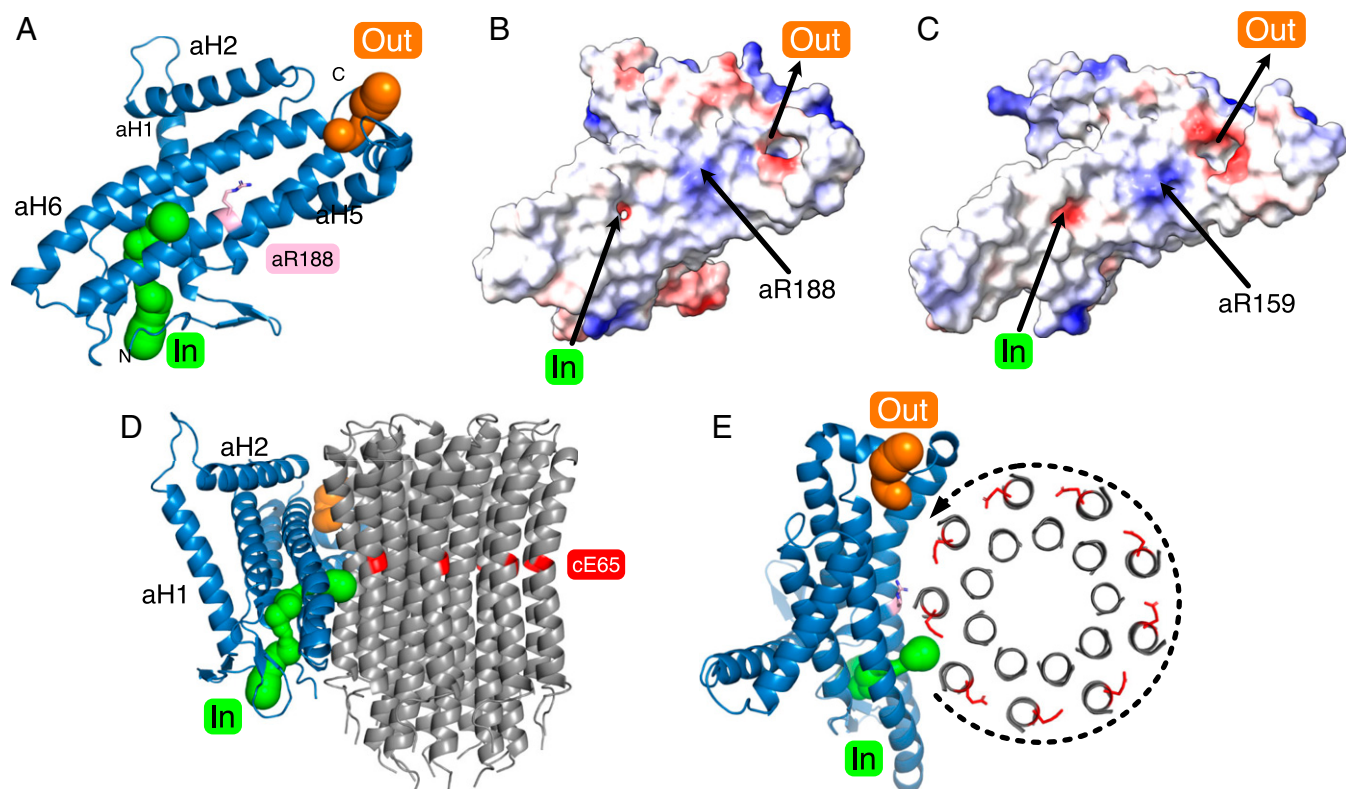


**Fig. 6.** Proton half-channels in the ATP synthase from *M. smegmatis*. (A) The a-subunit (blue) viewed from approximately the center of the  $c_9$ -ring toward the lipid bilayer. The inlet and outlet proton half-channels depicted by green and orange spheres, respectively, contain polar residues in the otherwise hydrophobic protein. The essential residue aArg188, located between the two half-channels, deprotonates the carboxylic groups of cGlu65 residues as they are rotated into the inlet half-channel. (B and C) Comparison of the electrostatic surfaces of the a-subunits from *M. smegmatis* and *Bos taurus*, respectively, illustrating the similar locations of the inlet and outlets of the two half-channels. The electrostatic range is  $-10$  (red),  $0$  (white),  $+10$  (blue). (D and E) Views, respectively, of the a-subunit (blue) from inside and from above the plane of the bacterial IPM from the cytoplasmic side showing its spatial relationship to the  $c_9$ -ring (in cartoon representation in D and showing cross-sections of  $\alpha$ -helices in E). Protons enter the inlet channel (green) from the periplasm, passing between  $\alpha$ -helices aH5 and aH6 and onto the negatively charged carboxyl of a cE65 residue. The protonation of a cE65 at the inlet is accompanied by the deprotonation of a cE65 residue in the outlet half-channel. The application of the pmf to the  $c_9$ -ring via the Grothuss water chain in the inlet channel (not resolved) rotates the  $c_9$ -ring in the anticlockwise direction as viewed from above.

arms of L-shaped inlet half-channel plus aAsn192 close to aGly196 and aArg188, and aTyr240 which is between aArg188 and the other residues of the outlet channel (see Fig. 6 and *SI Appendix*, Fig. S21).

**Potential Drug Targets.** The present structure of the ATP synthase from *M. smegmatis* confirms the site of binding of BD described previously and also defines three unique features that have the potential to be exploited in the design of new inhibitors that could be developed into novel drugs against TB. The first of these sites involves the “hook” and “catch” features involved in the ATP hydrolytic inhibitory mechanism, described also in the prior structure. The second is the “fail-safe” device that is likely to enhance the engagement of the hook and loop in state S1. The third is the unique mode of association of the PS with the N-terminal regions of the  $\alpha$ -subunits. The “hook and catch” device could be locked in place by small molecules that bind to both features, thereby preventing synthesis of ATP. The “fail-safe” interaction could either be augmented by a small molecule binding across the feature, or its formation could be impeded by small molecules binding to its two elements. Compounds with the features of suitably designed “molecular glues” (29) might enhance the stability of both features and be effective inhibitors of ATP synthesis by the enzyme. The third target would require small molecules that would impede the attachment of the PS to the  $F_1$ -domain

during its assembly, thereby preventing the coupling of the pmf to the synthesis of ATP. Once such inhibitors had been identified, then would follow the extensive process of converting them into effective drugs for treating TB.

## Materials and Methods

The mycobacterial ATP synthase was overexpressed in *M. smegmatis* mc<sup>2</sup>4517 from a plasmid containing the entire *atp* operon from *M. smegmatis* mc<sup>2</sup>155 modified to encode a b'-subunit with a C-terminal His<sub>10</sub>-tag. The enzyme was extracted from broken cells with buffer containing 1% (wt/vol) 4-trans(4-transpropylcyclohexyl)-cyclohexyl- $\alpha$ -maltoside and purified by metal affinity chromatography. The subunits of the enzyme were characterized by mass spectrometry. The purified enzyme was applied to electron microscopy grids, and high-resolution cryo-EM data were collected with a Titan Krios instrument. ATP synthase particles were picked with crYOLO (30), and a variety of related structures were determined by hierarchical classification and refinement with RELION (31). The resolution and interpretability of specific regions of the maps were improved by focused local refinement of the membrane domain, the membrane extrinsic catalytic domain, the PS, the stator and the b $\delta$ -subunit, and these subregion reconstructions were assembled together into composite structures and refined into atomic models. Merging of substate particle sets at the expense of substate distinction improved the resolutions in the  $F_1$ , membrane, rotor, and b $\delta$  domains, and reclassification of all particle data at the expense of rotational state distinction, while masking the membrane domain, revealed the presence of BD. Fourier shell correlation curves and local resolution estimations were calculated with RELION. Model building into focused maps was performed with Coot (32), and real space refinement with PHENIX (33–35). The starting model comprised the crystal

structures of the F<sub>1</sub>-domain of *M. smegmatis* ATP synthase (PDB ID code 6FOC) (6) and the c<sub>9</sub>-ring in the presence (PDB ID code 4V1F) and absence of BD (PDB ID code 4V1G) (5). All other subunits were built de novo. Model geometry and density fit validation were performed by MolProbity (36, 37) and EMRinger (38), respectively.

**Data Availability.** Protein models and electron density map data have been deposited in the Protein Data Bank and the Electron Microscopy Data Bank under the following accession numbers: 7NJK (EMD-12377–12381), 7NJL (EMD-12382–12386), 7NJM (EMD-12387–12391), 7NJJ (EMD-12392–12396), 7NJO (EMD-12397–12401), 7NJP (EMD-12402–12406), 7NJK (EMD-12407–12411),

7NJR (EMD-12412–12416), 7NJS (EMD-12417–12421), 7NJT (EMD-12422), 7NJU (EMD-12423), 7NJV (EMD-12424), 7NJW (EMD-12425), 7NXX (EMD-12426), 7NJJ (EMD-12427), 7NK7 (EMD-12432), 7NK9 (EMD-12434), 7NKB (EMD-12436), 7NKD (EMD-12438), 7NKH (EMD-12439), 7NKP (EMD-12404), 7NKK (EMD-12442), 7NKL (EMD-12406), 7NKJ (EMD-12441), 7NL9 (EMD-12461), 7NKN (EMD-12444), and 7NKQ (EMD-12446).

**ACKNOWLEDGMENTS.** This work was supported by the Medical Research Council via grants MR/M009858/1 and MC\_UU\_00015/8 (to J.E.W.). We thank Y. Chaban, A. Siebert, and staff of eBIC, Diamond Light Source for expert operation of microscopes and advice on data collection.

1. T. V. A. Nguyen *et al.*, Bedaquiline resistance: Its emergence, mechanism, and prevention. *Clin. Infect. Dis.* **66**, 1625–1630 (2018).
2. M. Luo *et al.*, Bedaquiline inhibits the yeast and human mitochondrial ATP synthases. *Commun. Biol.* **3**, 452 (2020).
3. L. Chiaradia *et al.*, Dissecting the mycobacterial cell envelope and defining the composition of the native mycomembrane. *Sci. Rep.* **7**, 12807 (2017).
4. J. E. Walker, The ATP synthase: The understood, the uncertain and the unknown. *Biochem. Soc. Trans.* **41**, 1–16 (2013).
5. L. Preiss *et al.*, Structure of the mycobacterial ATP synthase F<sub>o</sub> rotor ring in complex with the anti-TB drug bedaquiline. *Sci. Adv.* **1**, e1500106 (2015).
6. A. T. Zhang, M. G. Montgomery, A. G. W. Leslie, G. M. Cook, J. E. Walker, The structure of the catalytic domain of the ATP synthase from *Mycobacterium smegmatis* is a target for developing antitubercular drugs. *Proc. Natl. Acad. Sci. U.S.A.* **116**, 4206–4211 (2019).
7. J. E. Walker, V. K. Dickson, The peripheral stalk of the mitochondrial ATP synthase. *Biochim. Biophys. Acta* **1757**, 286–296 (2006).
8. P. Lu, H. Lill, D. Bald, ATP synthase in mycobacteria: Special features and implications for a function as drug target. *Biochim. Biophys. Acta* **1837**, 1208–1218 (2014).
9. E. Morales-Rios, M. G. Montgomery, A. G. W. Leslie, J. E. Walker, Structure of ATP synthase from *Paracoccus denitrificans* determined by X-ray crystallography at 4.0 Å resolution. *Proc. Natl. Acad. Sci. U.S.A.* **112**, 13231–13236 (2015).
10. M. Sobti *et al.*, Cryo-EM structures of the autoinhibited *E. coli* ATP synthase in three rotational states. *eLife* **5**, e21598 (2016).
11. H. Guo, T. Suzuki, J. L. Rubinstein, Structure of a bacterial ATP synthase. *eLife* **8**, 43128 (2019).
12. W. Junge, H. Sielaff, S. Engelbrecht, Torque generation and elastic power transmission in the rotary F<sub>o</sub>F<sub>1</sub>-ATPase. *Nature* **459**, 364–370 (2009).
13. M. Allegretti *et al.*, Horizontal membrane-intrinsic  $\alpha$ -helices in the stator a-subunit of an F-type ATP synthase. *Nature* **521**, 237–240 (2015).
14. H. Guo *et al.*, Structure of mycobacterial ATP synthase bound to the tuberculosis drug bedaquiline. *Nature* **589**, 143–147 (2021).
15. T. E. Spikes, M. G. Montgomery, J. E. Walker, Structure of the dimeric ATP synthase from bovine mitochondria. *Proc. Natl. Acad. Sci. U.S.A.* **117**, 23519–23526 (2020).
16. S. H. Roh *et al.*, Cryo-EM and MD infer water-mediated proton transport and autoinhibition mechanisms of V<sub>o</sub> complex. *Sci. Adv.* **6**, eabb9605 (2020).
17. M. Sobti *et al.*, Cryo-EM structures provide insight into how *E. coli* F<sub>1</sub>F<sub>o</sub> ATP synthase accommodates symmetry mismatch. *Nat. Commun.* **11**, 2615 (2020).
18. D. Pogoryelov, O. Yildiz, J. D. Faraldo-Gómez, T. Meier, High-resolution structure of the rotor ring of a proton-dependent ATP synthase. *Nat. Struct. Mol. Biol.* **16**, 1068–1073 (2009).
19. H. Sielaff, T. M. Duncan, M. Börsch, The regulatory subunit  $\epsilon$  in *Escherichia coli* F<sub>o</sub>F<sub>1</sub>-ATP synthase. *Biochim. Biophys. Acta Bioenerg.* **1859**, 775–788 (2018).
20. W. G. Saw *et al.*, Disrupting coupling within mycobacterial F-ATP synthases subunit  $\epsilon$  causes dysregulated energy production and cell wall biosynthesis. *Sci. Rep.* **9**, 16759 (2019).
21. C. F. Wong *et al.*, A systematic assessment of mycobacterial F<sub>1</sub>-ATPase subunit  $\epsilon$ 's role in latent ATPase hydrolysis. *FEBS J.* **288**, 818–836 (2021).
22. I. N. Watt, M. G. Montgomery, M. J. Runswick, A. G. W. Leslie, J. E. Walker, Bioenergetic cost of making an adenosine triphosphate molecule in animal mitochondria. *Proc. Natl. Acad. Sci. U.S.A.* **107**, 16823–16827 (2010).
23. T. E. Spikes, M. G. Montgomery, J. E. Walker, Interface mobility between monomers in dimeric bovine ATP synthase participates in the ultrastructure of inner mitochondrial membranes. *Proc. Natl. Acad. Sci. U.S.A.* **118**, e2021012118 (2021).
24. A. Hotra *et al.*, Deletion of a unique loop in the mycobacterial F-ATP synthase  $\gamma$  subunit sheds light on its inhibitory role in ATP hydrolysis-driven H<sup>+</sup> pumping. *FEBS J.* **283**, 1947–1961 (2016).
25. A. L. Cozens, J. E. Walker, The organization and sequence of the genes for ATP synthase subunits in the cyanobacterium *Synechococcus* 6301. Support for an endosymbiotic origin of chloroplasts. *J. Mol. Biol.* **194**, 359–383 (1987).
26. H. S. Van Walraven, R. Lutter, J. E. Walker, Organization and sequences of genes for the subunits of ATP synthase in the thermophilic cyanobacterium *Synechococcus* 6716. *Biochem. J.* **294** (Pt 1), 239–251 (1993).
27. A. L. Cozens, J. E. Walker, A. L. Phillips, A. K. Huttly, J. C. Gray, A sixth subunit of ATP synthase, an F<sub>o</sub> component, is encoded in the pea chloroplast genome. *EMBO J.* **5**, 217–222 (1986).
28. J. E. Walker, M. J. Runswick, M. Saraste, Subunit equivalence in *Escherichia coli* and bovine heart mitochondrial F<sub>1</sub>F<sub>o</sub> ATPases. *FEBS Lett.* **146**, 393–396 (1982).
29. S. L. Schreiber, The rise of molecular glues. *Cell* **184**, 3–9 (2021).
30. T. Wagner *et al.*, SPHIRE-crYOLO is a fast and accurate fully automated particle picker for cryo-EM. *Commun. Biol.* **2**, 218 (2019).
31. J. Zivanov *et al.*, New tools for automated high-resolution cryo-EM structure determination in RELION-3. *eLife* **7**, e42166 (2018).
32. P. Emsley, B. Lohkamp, W. G. Scott, K. Cowtan, Features and development of Coot. *Acta Crystallogr. D Biol. Crystallogr.* **66**, 486–501 (2010).
33. P. V. Afonine *et al.*, Real-space refinement in PHENIX for cryo-EM and crystallography. *Acta Crystallogr. D Struct. Biol.* **74**, 531–544 (2018).
34. P. V. Afonine *et al.*, New tools for the analysis and validation of cryo-EM maps and atomic models. *Acta Crystallogr. D Struct. Biol.* **74**, 814–840 (2018).
35. D. Liebschner *et al.*, Macromolecular structure determination using X-rays, neutrons and electrons: Recent developments in Phenix. *Acta Crystallogr. D Struct. Biol.* **75**, 861–877 (2019).
36. I. W. Davis *et al.*, MolProbity: All-atom contacts and structure validation for proteins and nucleic acids. *Nucleic Acids Res.* **35**, W375–83 (2007).
37. V. B. Chen *et al.*, MolProbity: All-atom structure validation for macromolecular crystallography. *Acta Crystallogr. D Biol. Crystallogr.* **66**, 12–21 (2010).
38. B. A. Barad *et al.*, EMRinger: Side chain-directed model and map validation for 3D cryo-electron microscopy. *Nat. Methods* **12**, 943–946 (2015).